Sensorless Control With Switching Frequency Square Wave Voltage Injection for SPMSM With Low Rotor Magnetic Anisotropy

Alessandro Benevieri, Andrea Formentini, *Member, IEEE*, Mario Marchesoni, *Member, IEEE*, Massimiliano Passalacqua, *Member, IEEE*, and Luis Vaccaro, *Member, IEEE*

***Abstract*—High-frequency signal injection sensorless algorithms are widely studied and used for rotor angle estimation in permanent magnet synchronous motor (PMSM) at low speed or standstill. One of the main drawbacks of such methods is the acoustic noise connected to the voltage injection. In order to minimize this problem, it is advisable to increase the frequency of the injected signal. Thus, many studies focus on square-wave injection at the switching frequency, which is the maximum theoretical frequency. Since these methods exploit the rotor magnetic anisotropy, it is relatively easy to use them in interior PMSMs, where the rotor anisotropy is high. On the contrary, it is hard to exploit them in surface PMSMs, which have an almost symmetric rotor, although a low rotor magnetic anisotropy is still present. In this article, a sensorless algorithm with switching frequency square-wave injection is developed for surface PMSMs. To increase the signal-to-noise ratio, current oversampling is exploited. The benefits of such a technique are demonstrated with experimental results on a 2 N·m SPMSM.**

***Index Terms*—High-frequency (HF) injection, sensorless control, surface permanent magnet synchronous motor (SPMSM), square-wave injection.**

I. Introduction

PERMANENT magnet synchronous motors (PMSMs) are achieving increasing importance in various sectors thanks to their features: high torque-to-inertia ratio, high torque density and low maintenance.

According to the rotor construction, PMSMs can be divided in two main categories: motors with magnets mounted on rotor surface (surface PMSM, SPMSM) and motors with magnets mounted inside the rotor (interior PMSM, IPMSM).

The different position of the magnets influences the rotor magnetic symmetry. Indeed, SPMSM rotor is almost symmetric from a magnetic point of view, i.e., the direct axis inductance (*Ld*) is almost equal to the quadrature axis inductance (*Lq*). On the contrary, IPMSM are characterized by rotor anisotropy, i.e., *Ld* value is lower than Lq value.

One of the main drawbacks of PMSM is that rotor position is needed in order to realize a proper control [usually a field-oriented control (FOC)]. This measure can be obtained using encoders, resolvers, or Hall effect probes. However, the use of such transducers is related to some disadvantages, the main of which are the cost increase, the machine size increase, and the reliability reduction. For this reason, many studies focus on rotor angle estimation, in order to eliminate the position sensor; thus, such techniques are known as sensorless algorithms.

Sensorless controls can be divided in two main groups: passive methods and active methods.

Passive methods are based on estimators and exploit the machine model to determine rotor angle. Various techniques have been proposed so far. Disturbance observers for back electromotiveforce (back EMF) estimation are developed in [1], [2], and [3], a reduced-order extended Kalman filter is proposed in [4], [5], [6], and [7], whereas sliding-mode observers are exploited in [8], [9]. Other passive methods are based, instead, on rotor flux estimation [10], [11]. All above-mentioned techniques are characterized by performance degradation in the low-speed region since the back EMF tends to zero while speed approaches zero.

For this reason, active methods are used in the low-speed region. These methods exploit the rotor anisotropy by injecting a high-frequency (HF) voltage and demodulating the corresponding HF measured current.

The HF voltage can be injected in the stationary reference frame (rotating HF injection) [12], [13], [14] or in the synchronous reference frame (pulsating HF injection) [15], [16], [17], [18], [19].

The HF injection is connected to various drawbacks, e.g., additional losses, torque ripple, and acoustic noise. In various applications, the additional acoustic noise caused by the HF injection could be intolerable. Since the acoustic noise is significantly reduced if the injection frequency is increased, many studies focus on frequency increase. If a single current sample and a single PWM update are performed for each PWM period, the maximum frequency is achievable by injecting a square wave with a frequency equal to half of the switching frequency

Manuscript received 31 March 2022; revised 30 August 2022, 24 December 2022, and 28 February 2023; accepted 22 April 2023. Date of publication 25 April 2023; date of current version 21 June 2023. Recommended for publication by Associate Editor T. Shi. *(Corresponding author: Mario Marchesoni.)*

The authors are with the Electrical, Electronics and Telecommunication Engineering and Naval Architecture Department (DITEN), University of Genova, 16145 Genova, Italy (e-mail: alessandro.benevieri@edu.unige.it; andrea.formentini@unige.it; marchesoni@unige.it; massimiliano.passalacqua@unige.it; luis.vaccaro@unige.it).

Color versions of one or more figures in this article are available at https://doi.org/10.1109/TPEL.2023.3270357.

Digital Object Identifier 10.1109/TPEL.2023.3270357

(fsw/2) [20], [21], [22], [23]. If double sample/double update is performed, a square wave with a frequency equal to fsw can be injected [24], [25].

As it will be shown in Section II, the current component containing the angle information is proportional to the anisotropy ratio [i.e., (*Lq*-*Ld*)/*Lq*], thus, the higher is the difference between *Lq* and *Ld*, the easier is to estimate precisely the rotor position. For this reason, HF voltage injection methods are particularly suitable for IPMSMs.

The studies considering square-wave voltage injection at fsw/2 and fsw [20], [21], [22], [23], [24], [25] are all carried out on IPMSM. On the contrary, fsw square-wave injection on SPMSM is not investigated in the technical literature. Indeed, this is a particularly hard task, since the anisotropy ratio is very limited. The anisotropy ratio was equal to 46% for the motor considered during experimental tests in [20], 67% in [21], 54% in [22], 40% in [23], 21% in [24] and 33% in [25].

Several articles deal with sensorless control exploiting PWM ripple and measuring the current derivative with a measure oversampling [26], [27], [28], [29]. The current derivative evaluation can be performed during an active voltage vector [26] or during a zero voltage state [27]; in [28] the current derivative is calculated during the longer state, which can be an active vector or a zero vector depending on the working point. Nevertheless, also this technique is carried out on motors with high anisotropy ratio: 22% in [26], 78% in [28] and 17% in [29]. In [27], an SPMSM is considered, however a highly precise sigma-delta measuring system is needed. Although it is very low, magnetic anisotropy is also present in SPMSM motors. Indeed, there is still a slight asymmetry where the magnets are attached to the rotor and, furthermore, the magnetic permeability of magnets is not exactly the same as that of air.

In this article, differently from the above cited works, a SPMSM with about a 10% anisotropy ratio, evaluated at 5 kHz, is considered. Therefore, there is a significant problem connected to the signal-to-noise ratio of current measurements. This aspect is particularly critical since in this article standard industrial LEM sensors are used instead of high-precision sensors, in order to test algorithm robustness.

To overcome this problem, a new demodulation method with current oversampling while using square-wave voltage injection is proposed in this article exploiting field programmable gate array (FPGA) use. Current measurements with the double sample and with the oversample are compared. Then, a FOC is implemented exploiting the rotor angle estimation with the current oversample.

The rest of this article is organized as follows. The estimation algorithm is described in Section II. The experimental test bench is shown in Section III, whereas the experimental results are reported in Section IV. Finally, conclusion is carried out in Section V.

II. Estimation Algorithm

A. Principle of High-Frequency Pulsating Injection

PMSM equation in the rotor (synchronous) reference frame is shown in

$$\begin{bmatrix} v_d^r \\ v_q^r \end{bmatrix} = R_s \begin{bmatrix} i_d^r \\ i_q^r \end{bmatrix} + \begin{bmatrix} L_d & 0 \\ 0 & L_q \end{bmatrix} \frac{d}{dt} \begin{bmatrix} i_d^r \\ i_q^r \end{bmatrix} + \omega_r \begin{bmatrix} 0 & -L_q \\ L_d & 0 \end{bmatrix} \begin{bmatrix} i_d^r \\ i_q^r \end{bmatrix} + \omega_r \lambda_f \begin{bmatrix} 0 \\ 1 \end{bmatrix} \quad (1)$$

where $[v_d^r,\ v_q^r]^T$ and $[i_d^r,\ i_q^r]^T$ are the stator voltage and current components in the rotor reference frame, L_d and L_q are the d-axis and q-axis inductances, ω_r is the rotor speed, and λ_f is the permanent-magnet flux linkage.

If a HF voltage is injected in the rotor reference frame, the stator resistance can be neglected, since the terms $L_d \frac{di_d^r}{dt}$ and $L_q \frac{di_q^r}{dt}$ are significantly higher in comparison to the $R_s i_d^r$ and $R_s i_q^r$ ones. Moreover, since the HF voltage injection is exploited in the low-speed region, the rotor speed ω_r is negligible in comparison to the injected voltage frequency. Therefore, (1) can be simplified in (2)

$$\begin{bmatrix} v_{dh}^r \\ v_{qh}^r \end{bmatrix} = \begin{bmatrix} L_d & 0 \\ 0 & L_q \end{bmatrix} \frac{d}{dt} \begin{bmatrix} i_{dh}^r \\ i_{qh}^r \end{bmatrix} \quad (2)$$

where $[v_{dh}^r,\ v_{qh}^r]^T$ and $[i_{dh}^r,\ i_{qh}^r]^T$ are the HF voltage and current components. From (2), one can obtain as

$$\begin{bmatrix} i_{dh}^r \\ i_{qh}^r \end{bmatrix} = \int \begin{bmatrix} L_d & 0 \\ 0 & L_q \end{bmatrix}^{-1} \begin{bmatrix} v_{dh}^r \\ v_{qh}^r \end{bmatrix} dt. \quad (3)$$

In this article, the HF voltage is injected in the d-axis (pulsating HF injection). Since the rotor position is unknown, it is necessary to distinguish between the real rotor reference frame (RRF) and the estimated rotor reference frame (ERF).

The rotor angle error between the RRF and the ERF can be defined as

$$\tilde{\theta}_r = \theta_r - \hat{\theta}_r. \quad (4)$$

The HF voltage is injected in the ERF d-axis, as shown in

$$\begin{bmatrix} v_{dh}^{\hat{r}} \\ v_{qh}^{\hat{r}} \end{bmatrix} = V_h \begin{bmatrix} \cos \omega_h t \\ 0 \end{bmatrix} \quad (5)$$

where $[v_{dh}^{\hat{r}},\ v_{qh}^{\hat{r}}]^T$ are the HF voltage components in the ERF, V_h is the amplitude of the injected voltage and ω_h is the frequency of the injected voltage.

Since it exists an angle error $\tilde{\theta}_r$ between the RRF and the ERF, the voltage injection in the RRF is given by (6), from which it derives (7)

$$\begin{bmatrix} v_{dh}^r \\ v_{qh}^r \end{bmatrix} = \begin{bmatrix} \cos \tilde{\theta}_r & \sin \tilde{\theta}_r \\ -\sin \tilde{\theta}_r & \cos \tilde{\theta}_r \end{bmatrix} V_h \begin{bmatrix} \cos \omega_h t \\ 0 \end{bmatrix} \quad (6)$$

$$\begin{bmatrix} v_{dh}^r \\ v_{qh}^r \end{bmatrix} = V_h \begin{bmatrix} \cos \tilde{\theta}_r \cos \omega_h t \\ -\sin \tilde{\theta}_r \cos \omega_h t \end{bmatrix}. \quad (7)$$

The current components $[i_{dh}^{\hat{r}},\ i_{qh}^{\hat{r}}]$ in the ERF are related to the current components in the RRF by (8). Substituting (3) in (8), one obtains (9)

$$\begin{bmatrix} i_{dh}^{\hat{r}} \\ i_{qh}^{\hat{r}} \end{bmatrix} = \begin{bmatrix} \cos \tilde{\theta}_r & -\sin \tilde{\theta}_r \\ \sin \tilde{\theta}_r & \cos \tilde{\theta}_r \end{bmatrix} \begin{bmatrix} i_{dh}^r \\ i_{qh}^r \end{bmatrix} \quad (8)$$

$$\begin{bmatrix} i^{\hat{r}}_{dh} \\ i^{\hat{r}}_{qh} \end{bmatrix} = \begin{bmatrix} \cos\tilde{\theta}_r & -\sin\tilde{\theta}_r \\ \sin\tilde{\theta}_r & \cos\tilde{\theta}_r \end{bmatrix} \int \begin{bmatrix} L_d & 0 \\ 0 & L_q \end{bmatrix}^{-1} \begin{bmatrix} v^r_{dh} \\ v^r_{qh} \end{bmatrix} dt. \quad (9)$$

Substituting (6) into (9) and developing the calculations, one finally obtains

$$\begin{bmatrix} i^{\hat{r}}_{dh} \\ i^{\hat{r}}_{qh} \end{bmatrix} = \frac{V_h}{\omega_h} \begin{bmatrix} \left(\frac{\cos^2\tilde{\theta}_r}{L_d} + \frac{\sin^2\tilde{\theta}_r}{L_q}\right) \sin\omega_h t \\ \frac{1}{2}\left(\frac{\Delta L}{L_d L_q}\right) \sin 2\tilde{\theta}_r \sin\omega_h t \end{bmatrix} \quad (10)$$

where $\Delta L = L_q - L_d$.

From (10) one can demodulate the $i^{\hat{r}}_{qh}$ component as in

$$\varepsilon = i^{\hat{r}}_{qh} \sin(\omega_h t) = \left[\frac{V_h}{\omega_h}\frac{1}{2}\left(\frac{\Delta L}{L_d L_q}\right) \sin^2\omega_h t\right] \sin 2\tilde{\theta}_r. \quad (11)$$

For small errors, (12) is verified and therefore (11) can be approximated as in (13)

$$\sin(2\tilde{\theta}_r) \simeq 2\tilde{\theta}_r \quad (12)$$

$$\varepsilon \simeq \left[\frac{V_h}{\omega_h}\left(\frac{\Delta L}{L_d L_q}\right) \sin^2\omega_h t\right] \tilde{\theta}_r. \quad (13)$$

Since the quantity in the square bracket is always positive ε is proportional to $\tilde{\theta}_r$ and can be therefore used as feedback error to implement the rotor angle estimator.

B. Proposed Square-Wave Injection With Current Oversample

In this article, an ERF square wave is injected in the d-axis, as shown in (14)

$$\begin{bmatrix} v^{\hat{r}}_{dh} \\ v^{\hat{r}}_{qh} \end{bmatrix} = V_h \begin{bmatrix} -sign\frac{dcw(t)}{dt} \\ 0 \end{bmatrix} \quad (14)$$

where $cw = cw(t)$ is the PWM Carrier Wave which can be expressed as in (15)

$$cw(t) = 4\left|f_{cw}t - \left\lfloor f_{cw}t + \frac{1}{2}\right\rfloor\right| - 1 \quad (15)$$

where f_{cw} is the frequency of the carrier wave and $\lfloor\rfloor$ indicates the floor function. From (14), (16) follows:

$$\begin{bmatrix} v^r_{dh} \\ v^r_{qh} \end{bmatrix} = \begin{bmatrix} \cos\tilde{\theta}_r & \sin\tilde{\theta}_r \\ -\sin\tilde{\theta}_r & \cos\tilde{\theta}_r \end{bmatrix} V_h \begin{bmatrix} -\text{sign}\frac{dcw(t)}{dt} \\ 0 \end{bmatrix}. \quad (16)$$

Since (9) is valid for an arbitrary voltage injection and the relation in (17) can be verified, substituting (16) and (17) in (9) leads to (18)

$$\int sign\left[\frac{d\,cw(t)}{dt}\right] dt = \frac{cw}{4f_{sw}} \quad (17)$$

$$i^{\hat{r}}_{qh} = \left[\frac{V_h}{8f_{sw}}\left(\frac{\Delta L}{L_d L_q}\right)(-cw)\right] \cdot \sin 2\tilde{\theta}_r. \quad (18)$$

From (18) one can demodulate the $i^{\hat{r}}_{qh}$ component as in

$$\begin{aligned} \varepsilon &= i^{\hat{r}}_{qh} \sin\left(-cw\frac{\pi}{2}\right) \\ &= \left[\frac{V_h}{8f_{sw}}\left(\frac{\Delta L}{L_d L_q}\right)(-cw) \cdot \sin\left(-cw\frac{\pi}{2}\right)\right] \cdot \sin 2\tilde{\theta}_r. \end{aligned} \quad (19)$$

For small errors, (12) is valid and therefore (19) can be approximated as

$$\varepsilon \simeq \left[\frac{V_h}{4f_{sw}}\left(\frac{\Delta L}{L_d L_q}\right)(-cw)\sin(-cw\frac{\pi}{2})\right] \tilde{\theta}_r. \quad (20)$$

Since $cw \in [-1; 1]$, the quantity in the square bracket is always positive, thus ε is proportional to $\tilde{\theta}_r$ and can be therefore used as feedback error to implement the rotor angle estimator.

Injecting a square wave at fsw frequency, a double pulsewidth modulation (PWM) update is necessary for each period; moreover, at least two current samples must be performed in each PWM period [24].

As it can be noticed from (10), the $i^{\hat{r}}_{qh}$ component is proportional to the anisotropy ratio, i.e., $\Delta L/L_q$. Since this article focuses on SPMSMs, which are characterized by a very low anisotropy ratio, the $i^{\hat{r}}_{qh}$ fundamental component is considerably weak; as a consequence, the signal-to-noise ratio is weak.

In this article, current oversampling is proposed to increase the signal-to-noise ratio, as shown in the control scheme of Fig. 1. As a matter of fact, the noise in current measurements can be usually assumed as Gaussian white noise with zero mean; therefore, by oversampling the current measurements and calculating the average over one switching period, the noise decreases [26], [27], [28], [29]. In order to evaluate the effectiveness of the proposed solution, both the double sample per period technique (DS) and the oversampling technique (OS) are implemented and tested. The two different approaches are shown in Figs. 2 and 3. Please note that, since the fundamental frequency is significantly lower than the injection frequency, it can be considered as a constant during the switching period, therefore $i^{\hat{r}}_q$ can be used to estimated the angle instead of $i^{\hat{r}}_{qh}$. Indeed, the integration of a constant (low-frequency fundamental waveform) multiplied by the sine function (18), leads to zero contribution.

In both figures, the PWM carrier wave, the analog to digital converter (ADC) sample interrupt, the cw interrupt, the gate pulses and the $v^{\hat{r}}_{dh}$ are shown. Details on the experimental test bench are provided in Section III; however, oscilloscope acquisitions in Figs. 2 and 3 are here reported to explain the proposed technique.

In the DS, the currents are sampled on PWM carrier wave bottom and top, as it is shown in Fig. 2. In the OS, the current sample is performed each 1 μs (i.e., 200 samples per PWM period, being fsw equal to 5 kHz), as Fig. 3 shows.

In order to implement the proposed algorithm, a FPGA is exploited. In particular, the PWM carrier wave, the $v^{\hat{r}}_{dh}$ injection, the gate pulse signals, and the ADC interrupts are managed by the FPGA, as shown in Fig. 1. The ADC interrupts are generated each 1 μs in the OS and on carrier wave bottom and top in the DS. Moreover, (18) is implemented in the FPGA. As a matter of fact, for each ADC interrupt, a value of the error ε is calculated and integrated; the integrator is reset each carrier wave interrupt (cw interrupt). Since error ε is in FPGA arbitrary units, the integration output corresponds to the error average over the switching period, as indicated by the blue rectangle in Fig. 1. Please note that the cw interrupt is generated by the FPGA on the carrier wave rising zero crossing.

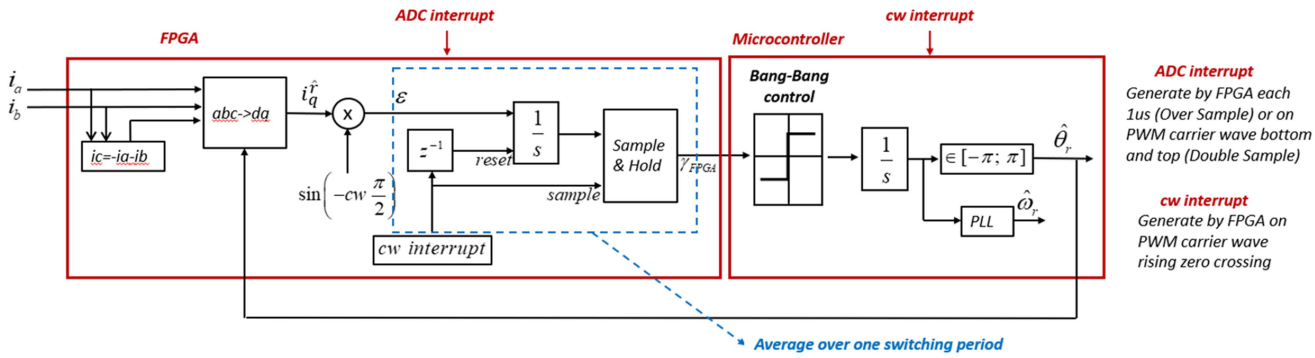

Fig. 1. HF voltage injection and rotor angle estimation algorithm.

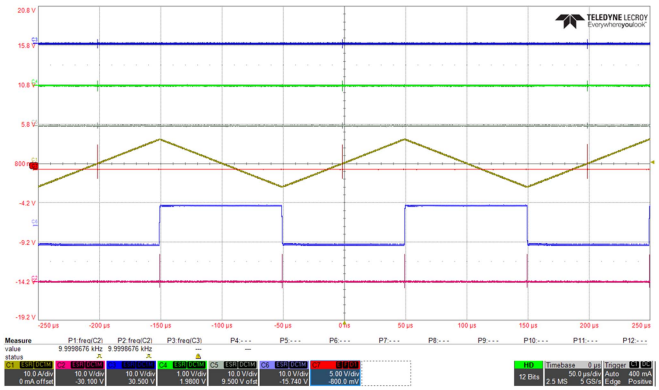

Fig. 2. Double sample per period. Gate pulses (blue, green and grey), PWM carrier wave (yellow), (violet), ADC sample interrupt (pink), and cw interrupt (red).

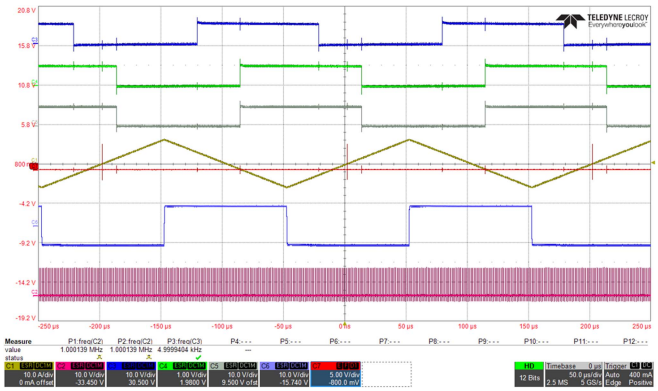

Fig. 3. Oversampling technique. Gate pulses (blue, green and grey), PWM carrier wave (yellow), (violet), ADC sample interrupt (pink), and cw interrupt (red).

The output of ε integrator is sampled each cw interrupt and the sample and hold output (γ_{FPGA}) is sent to the microcontroller. The signal is sent to a bang-bang control which gives as output -1 or $+1$, multiplied by an opportune gain. The bang-bang output corresponds to the estimated speed and the bang-bang gain is the maximum speed at which the control can work. Therefore, the estimated speed is integrated to obtain the estimated angle $\hat{\theta}_r$, which is used by the FPGA for current demodulation and by the FOC control implemented in the microcontroller. Since the output of the bang-bang control cannot be used as speed feedback in the FOC (indeed it provides only the maximum or the minimum speed value), a PLL is used to evaluate the estimated speed $\hat{\omega}_r$ from $\hat{\theta}_r$. The algorithm in the microcontroller is executed each cw interrupt, i.e., once per PWM period.

In terms of FPGA computational complexity, as can be noted from Fig. 1, the two most expensive operations are the currents *abc*-to-*dq* transformation and the sin(-cw π/2) calculation. Regarding the former, please note the angle $\hat{\theta}_r$ is updated at the microcontroller sampling frequency. For this reason the $\sin(\hat{\theta}_r)$ and $\cos(\hat{\theta}_r)$ quantities are calculated in the microcontroller and passed to the FPGA. In this way the *abc*-to-*dq* transformation reduces to 6 multiplications and 4 sums. Modern FPGAs are usually equipped with tens of multiplier making this operation not particularly computationally expensive. The sin(-cw π/2) operation is performed using a CORDIC algorithm. The latter works with integer numbers and return the results in a number of clock cycles equal to the number of bits used for number representation. In this article, a 32 bits representation is used. Also in this case 32 clock cycles are an acceptable delay compared to the 100 clock cycles available every sample time (sampling at 1 μs with an FPGA clock frequency of 100 MHz).

III. Test Bench

The control hardware used to perform the experimental tests is shown in Fig. 4. The algorithm is implemented in Dspace MicrolabBox, which integrates an FPGA and a microcontroller. Two currents are measured with 10 A LEMs. The gate pulses are sent as single-ended digital signals to a custom board which converts the signals to fiber optic signals used to control the inverter. In order to obtain the measurements shown in Figs. 2 and 3, the ADC interrupt drives a digital output, whereas the PWM carrier wave and the $v_{dh}^{\hat{r}}$ drive two analog outputs; please note that since conversion from FPGA units to volts is performed, the scales in Figs. 2 and 3 for such quantities are not significant. The gate signals are measured on the custom board with the oscilloscope. Dspace MicrolabBox has a resolver interface, which is used to

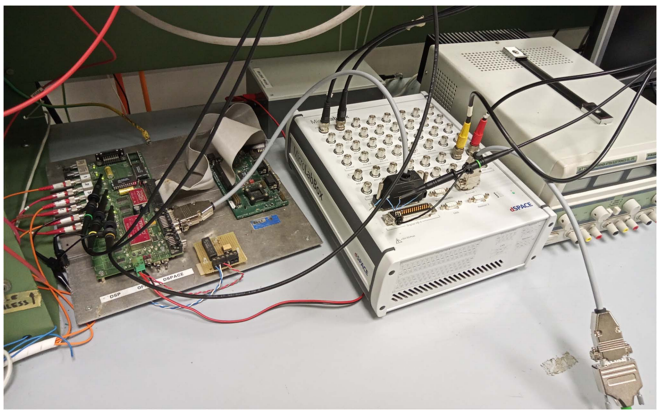

Fig. 4. Control hardware.

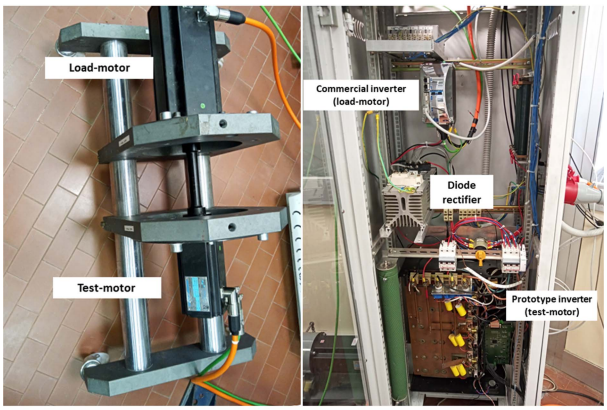

(a) (b)

(c)

Fig. 5. Experimental setup. (a) First motor test bench, (b) inverters, and (c) second motor test bench.

measure the rotor angle, in order to compare it with the estimated one.

The first motor test bench, used for tests presented in Section IV-A–IV-F, is shown in Fig. 5(a), a 2 N·m motor is used to test the proposed algorithm, whereas a 25.7 N·m motor simulates the load. The load motor has an encoder and can perform a precise sensored control, to provide the desired torque. A prototype inverter is used to control the tested motor, whereas a commercial inverter is used to control the load-motor and the torque reference is sent via Modbus to the inverter by Dspace. The parameters of the first test motor are given in Table I.

TABLE I
FIRST TEST MOTOR PARAMETERS

Parameter	Value
Rated torque	2 Nm
Rated speed	5000 rpm
Rated power	1.04 kW
Rated voltage	376V
Rated current	2.2 A
Pole pairs	4
Rated flux	0.147 Wb
Ld/Lq @ 5kHz	5.59/6.26 mH
Load-motor rated torque	25.7 Nm
Load-motor rated speed	2000 rpm
Load-motor drive maximum speed	2500 rpm

TABLE II
CONTROL PARAMETERS

Parameter	Value
Vh	100 V
Bang-bang gain	±200 rad/s
PLL kp	200
PLL ki	10000

TABLE III
SECOND TEST MOTOR PARAMETERS

Parameter	Value
Rated torque	10 Nm
Rated speed	1995 rpm
Rated power	2.09 kW
Rated voltage	376V
Rated current	3.6 A
Pole pairs	4
Rated flux	0.34 Wb
Ld/Lq @ 5kHz	4.9/5.3 mH
Load-motor rated torque	29 Nm
Load-motor rated speed	3000 rpm

L_d and L_q are measured with the LCR meter GW Instek LCR-817. The inverter used to supply the motor has 5 kHz switching frequency and 4 μs dead times; please note that this is quite high value. Dead times were not compensated on purpose, in order to test the algorithm robustness towards inverter nonlinearities.

The main parameters of the first load motor are also given in Table I. Control parameters are given in Table II. A second test bench equipped with a load cell able to measure the motor torque is used for tests presented in Section IV-G, since torque fluctuations are also evaluated in that case. The second test bench is shown in Fig. 5(c), while the parameters of the second test motor are given in Table III. The second test motor was connected to the same experimental setup and control hardware as the first one, and coupled with another SPMSM to provide the load torque when needed.

The injected voltage amplitude V_h is 100 V; this value is chosen empirically to obtain a good angle estimation as shown

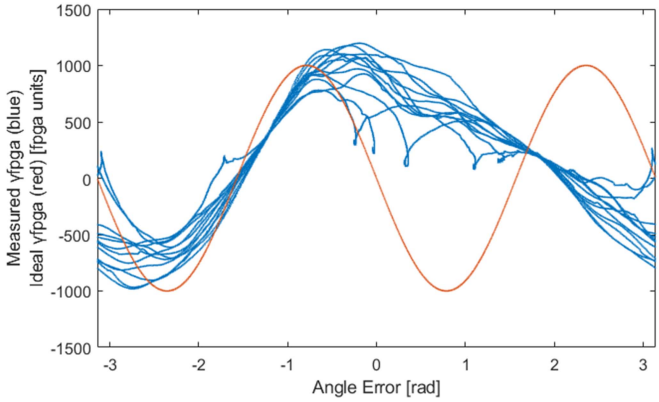

Fig. 6. γ_{FPGA} as a function of angle error, DS. Measured value (blue) and ideal value (red).

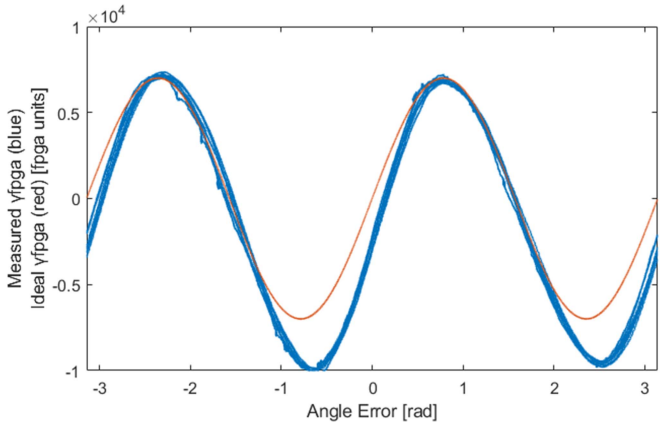

Fig. 7. γ_{FPGA} as a function of angle error, OS. Measured value (blue) and ideal value (red).

in Fig. 7. Please note that at standstill the maximum injectable voltage is $V_{\mathrm{dc}}/2$, i.e., approximately, 280 V. Therefore, there is a significant voltage margin in the low speed region, where the proposed algorithm is used, since 35% of V_{dc} /2 is injected. Moreover, the injected voltage amplitude is comparable with the values proposed in the technical literature. As a matter of fact, the injected voltage amplitude is 50 V in [20] for a 320 V-motor, 8 V with a 50 V dc-link (32% of *V*dc/2) in [21], 85 V for a 380 V-motor in [23] and 50 V with a 250 V dc-link (40% of $V_{\mathrm{dc}}/2$) in [24].

IV. Experimental Results

A. FGPA Output in Open-Loop

In order to verify the effectiveness of the proposed OS, in comparison to a traditional DS, the FPGA output γ_{FPGA}(i.e., the sample and hold output in Fig. 1) is measured with a fixed estimated angle ($\hat{\theta}_r$) and a variable rotor angle (θ_r). In other words, the microcontroller algorithm is disabled, the motor is moved by the coupled motor and a fixed $\hat{\theta}_r$ is used to perform the axis transformation from the measured currents (stationary reference frame) to the *dq*-currents (ERF); in this condition, γ_{FPGA}, which is proportional to the angle error, is measured. This test is performed for various angle $\hat{\theta}_r$; the case in which $\hat{\theta}_r = 0$ is shown in the following, just as an example.

Observing the $i_{qh}^{\hat{r}}$ expression in (20), applying the demodulation process of (19), it is easy to observe that γ_{FPGA} should be theoretically as in

$$\gamma_{\mathrm{FPGA}} = K \sin(2\tilde{\theta}_r) \tag{21}$$

where *K* depends on L_d, L_q, V_h, f_{sw}, on ADC conversion factor and on the number of samples per period. Therefore, *K* is a constant for each type of sampling method; as a matter of fact, it depends only on motor parameters, on HF voltage injection waveform, on the measurement hardware and on the number of samples per period.

The motor is turned several times with the external motor and the γ_{FPGA} is plotted as a function of the angle error, together with the ideal plot; γ_{FPGA} with the DS is shown in Fig. 6, whereas γ_{FPGA} with the OS is shown in Fig. 7.

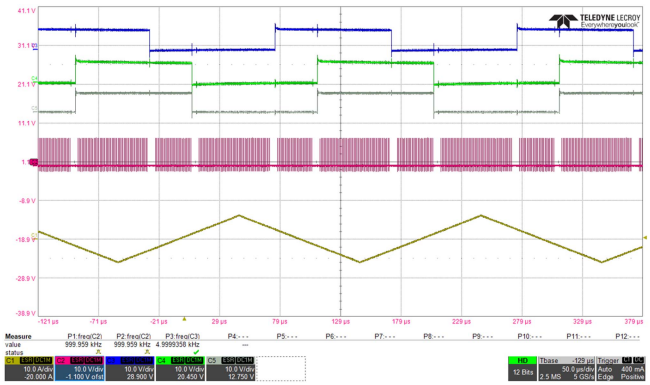

Fig. 8. Modified oversampling method. Gate pulses (blue, green, grey), PWM carrier wave (yellow), ADC sample interrupt (pink).

From Figs. 6 and 7, one can observe that the DS, which is usually exploited for IPMSM [24], cannot be used for SPMSM since the signal-to-noise ratio is too low and the effect of high order harmonics is predominant. On the contrary, the OS shows a good correspondence with the ideal behavior and just a small offset can be noted; in particular, the angle error at the zero crossing (which is the parameter that affects the estimation algorithm of Fig. 1) is moderate.

B. Current Oscillation During Turn On/Off Transients

In order to evaluate the effects of the current oscillations during turn ON/OFF transients, a modified oversampling method is tested, as reported in Fig. 8, where gate pulses (blue, green and grey), sample interrupt (pink) and carrier wave (yellow) are reported. Current sample is disactivated for 6 μs during the switching.

However, observing Fig. 9, one can note that the behavior with the modified oversampling method is worst than the behaviour shown in Fig. 7; moreover, the modified oversampling method is more complicated to be implemented and therefore it is not used for the experimental tests.

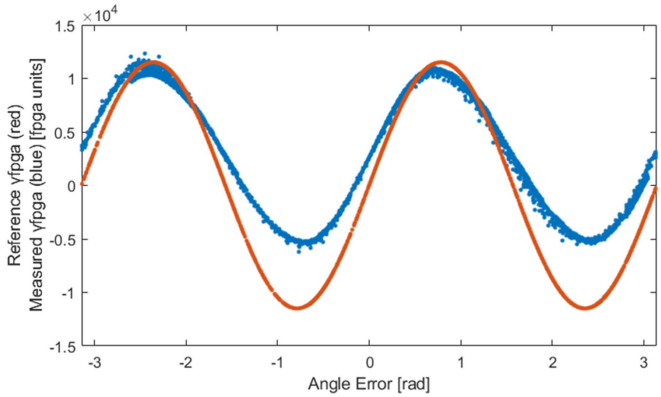

Fig. 9. γ_{FPGA} as a function of angle error, modified oversampling. Measured value (blue) and ideal value (red).

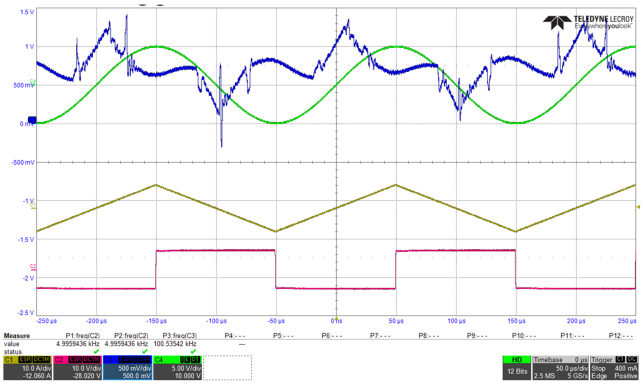

Fig. 10. *Iq* (blue), $\sin(cw \cdot \pi/2)$ (green), carrier wave (yellow), and *Vdh* (pink).

In order to better understand the effect of current oscillations during switching phase, the instantaneous *iq* value (calculated in the FPGA each 1 μs) is sent to a digital to analog converter (DAC) and acquired with the oscilloscope. *Iq* is shown in Fig. 10 (blue), together with the $\sin(cw \cdot \pi/2)$ (green), the carrier wave (yellow) and *Vdh* (pink). One can note a significant oscillation during the switching phase; however, only a few current samples are performed during this phase, and, therefore, the contribution of these samples in the integration process carried out over the entire switching period is limited.

C. Speed-Loop FOC Control. Speed Step in the Low-Speed Region

From the results shown in Fig. 6 it is clear that the DS cannot be used to implement a FOC control. In confirmation of that, a motor starting with no-load using DS was tested and failed. Moreover, motor starting to 250 r/min, using OS, is performed and then the control is switched to DS, causing the loss of angle estimation, as shown in Fig. 11.

Therefore, an FOC control is realized with the angle estimator shown in Fig. 1 and exploiting the OS. The initial polarity uncertainly is detected as shown in [23] and [30]. Reference and measured speed are shown in Fig. 12, where a test with speed

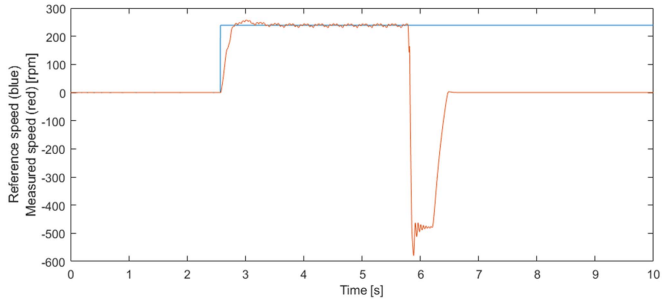

Fig. 11. Reference speed (blue) and measured speed (red). FOC control, no-load, starting with OS and switch to DS at 5.8 s.

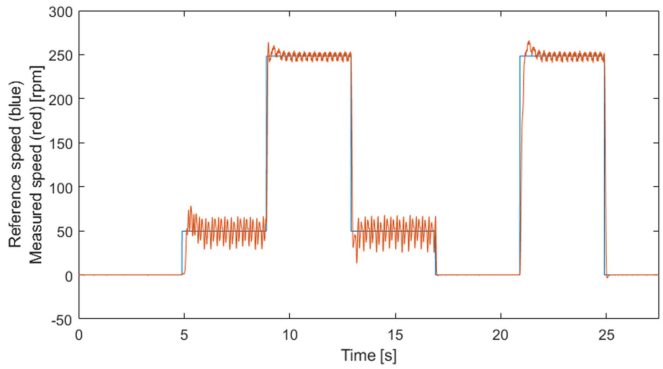

Fig. 12. Reference speed (blue) and measured speed (red). FOC control, no-load, OS.

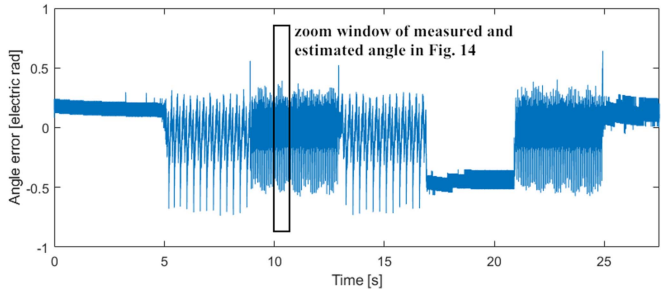

Fig. 13. Angle error. FOC control, no-load, OS.

steps without load is performed. The speed reference is set to 50 r/min (1% of the rated speed) and 250 r/min (5% of the rated speed). The corresponding angle error $\tilde{\theta}_r$ is shown in Fig. 13, whereas an enlargement of measured angle and estimated angle is shown in Fig. 14.

The same test is carried out with full-load. A full-load step is applied at standstill, then the motor is started with full-load and speed steps are performed.

Reference and measured speed for the full load test are shown in Fig. 15. The corresponding angle error $\tilde{\theta}_r$ is shown in Fig. 16, whereas an enlargement of the measured angle and estimated angle is shown in Fig. 17.

Even if a certain speed ripple can be seen, one has to note that the motor is working in the very-low speed region. Indeed the speed ripple at 50 r/min is about $\pm$20 r/min, which corresponds

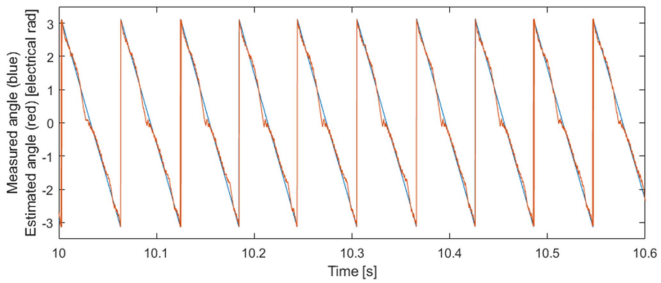

Fig. 14. Measured angle (blue) and estimated angle (red), enlargement. FOC control, no-load, OS.

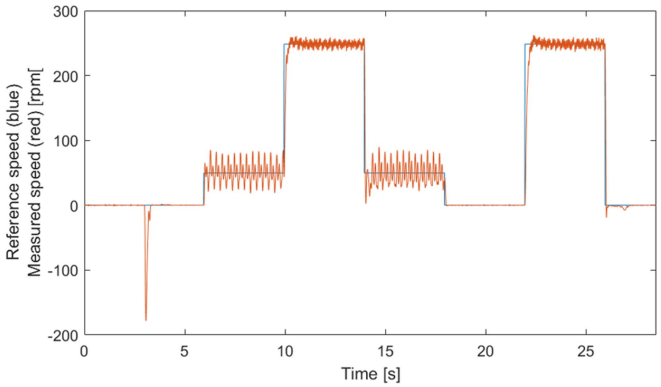

Fig. 15. Reference speed (blue) and measured speed (red). FOC control, full-load step at standstill, OS.

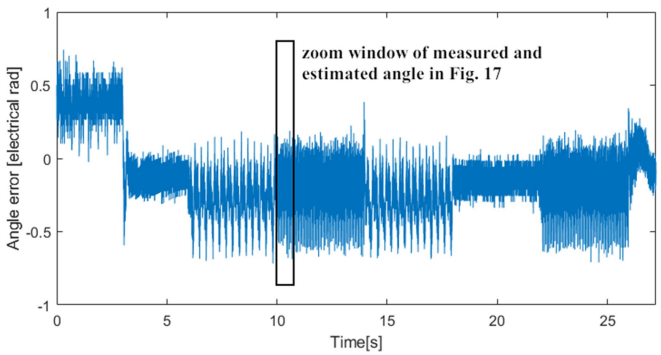

Fig. 16. Angle error. FOC control, full-load step at standstill, OS.

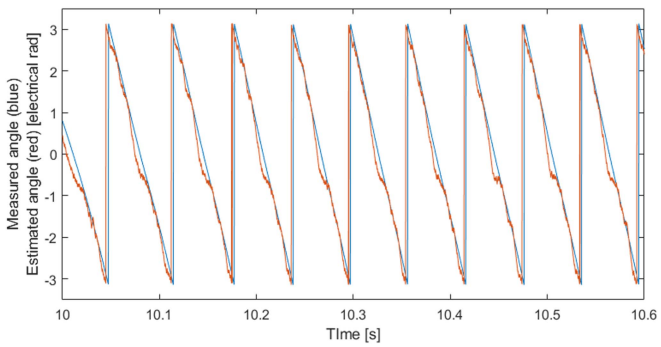

Fig. 17. Measured angle (blue) and estimated angle (red), enlargement. FOC control, full-load, OS.

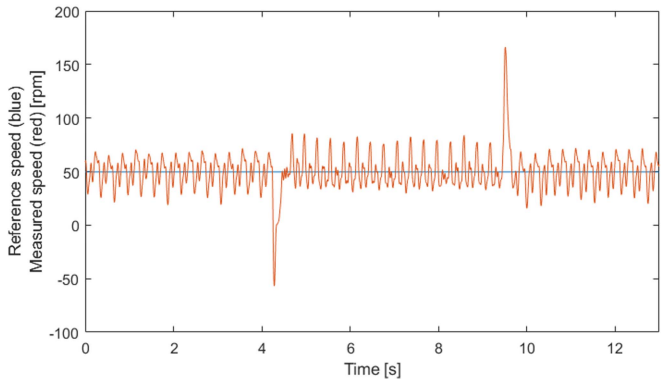

Fig. 18. Reference speed (blue) and measured speed (red). FOC control, load steps at 50 rpm, OS.

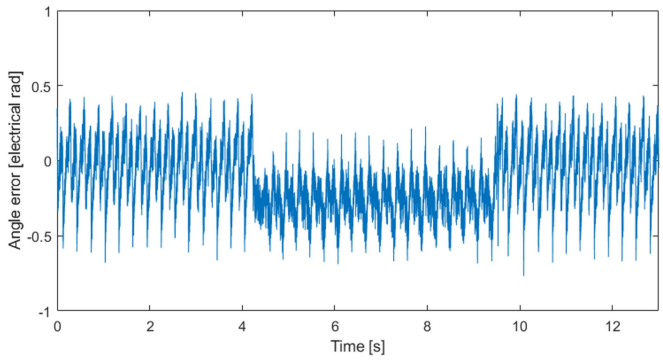

Fig. 19. Angle error. FOC control, load steps at 50 rpm, OS.

to $\pm$ 0.4% of the rated speed. Moreover, this method guarantees high robustness towards load perturbation at standstill and in the load-speed region (as demonstrated by the load step at standstill in Fig. 15), it allows to start the motor with full-load and it is then integrated with a model-based method for the medium-high speed region, where the motor usually works during steady-states as shown in Section IV-F.

D. Speed-Loop FOC Control. Load Step

A full-load step and a load release are applied both at 50 and 250 r/min. Reference and measured speed during load steps at 50 rpm are shown in Fig. 18, angle error is shown in Fig. 19, whereas a phase current is shown in Fig. 20. The same quantities are shown for the load step at 250 r/min in Figs. 21–23, respectively.

In both cases, the FOC control can face the load step and the estimation algorithm follows the rotor angle also during the load step.

E. Speed-Loop FOC Control. Sinusoidal Reference

Tests with a sinusoidal speed reference at 5 Hz are performed. In Fig. 24, reference and measured speed are shown in the no-load case, whereas the same plot is shown in Fig. 25 for the test

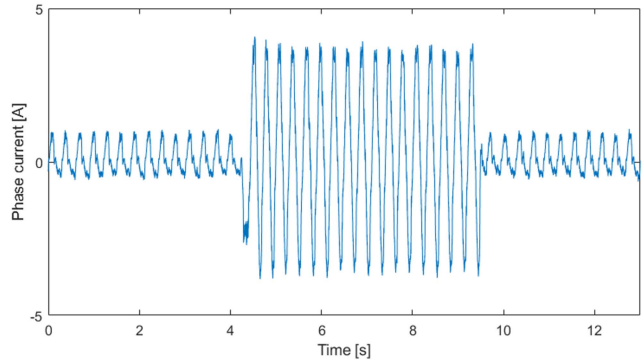

Fig. 20. Phase current. FOC control, load steps at 50 rpm, OS.

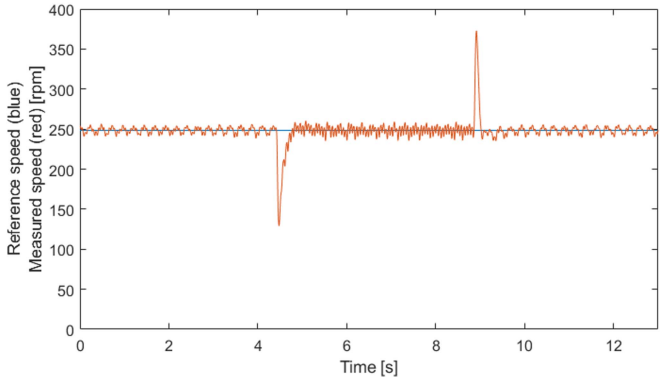

Fig. 21. Reference speed (blue) and measured speed (red). FOC control, load steps at 250 r/min, OS.

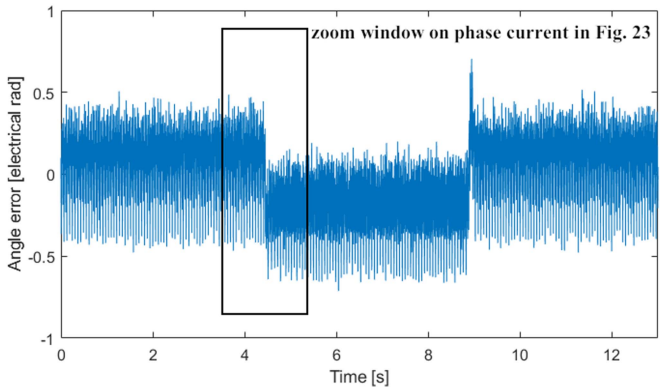

Fig. 22. Angle error. FOC control, load steps at 250 r/min, OS.

at full-load. From these results, one can note that the speed loop bandwidth is about 5 Hz.

F. Integration With a Model-Based Method for High-Speed

The proposed technique is particularly indicated for standstill and for the low speed region. However, for medium and high speed, a model-based method is more suitable, since it does not require any additional signal injection. For this reason, the proposed HF method is integrated with the rotor flux observer

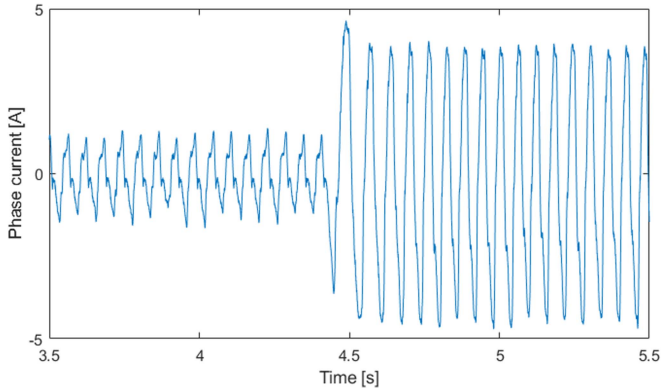

Fig. 23. Phase current. FOC control, load steps at 250 r/min, OS.

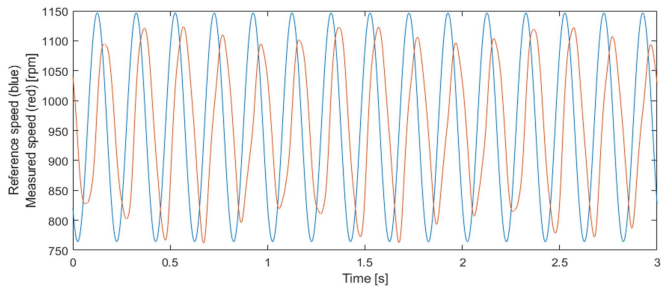

Fig. 24. Reference speed (blue) and measured speed (red). FOC control, 5 Hz speed reference, no-load, OS.

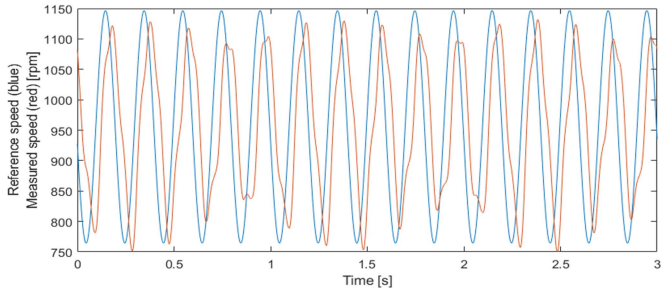

Fig. 25. Reference speed (blue) and measured speed (red). FOC control, 5 Hz speed reference, full load, OS.

(RFO) proposed in [10] which was proven to have high performance in a wide speed range [31].

The HF method is used until 350 r/min (7% of the rated speed) and then the algorithm switches to the RFO method.

In Fig. 26 motor starting with no-load is shown; 50, 250, and 5000 r/min (rated speed) steps are shown.

In Fig. 27, a full-load step is performed at standstill and then 50, 250, and 2500 r/min (50% of rated speed) steps are shown. Please note that the load motor drive maximum operating speed is 2500 r/min, therefore load steps can be performed only in this speed range.

In Fig. 28, a full load-step is applied at 350 r/min (HF method), then the reference speed is set to 355 r/min (RFO method) and a negative and then a positive full-load steps are performed.

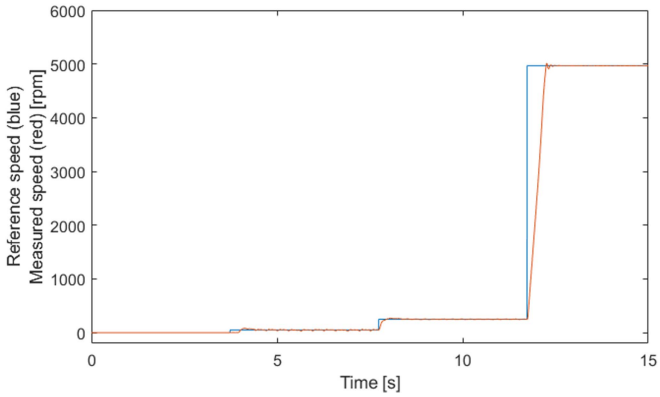

Fig. 26. Reference speed (blue) and measured speed (red). No-load, starting with HF and switch to RFO at 350 r/min.

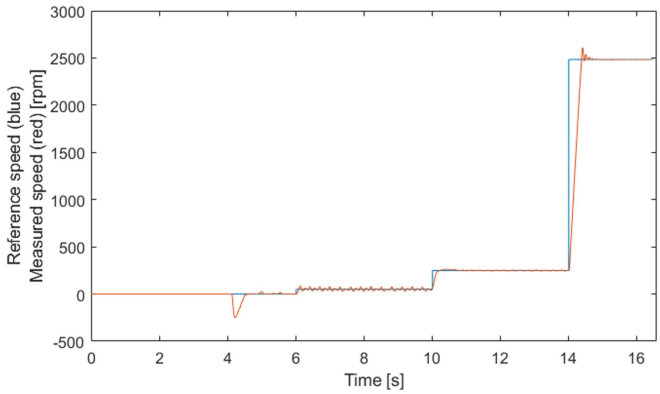

Fig. 27. Reference speed (blue) and measured speed (red). Full-load step at standstill, starting with HF and switch to RFO at 350 r/min.

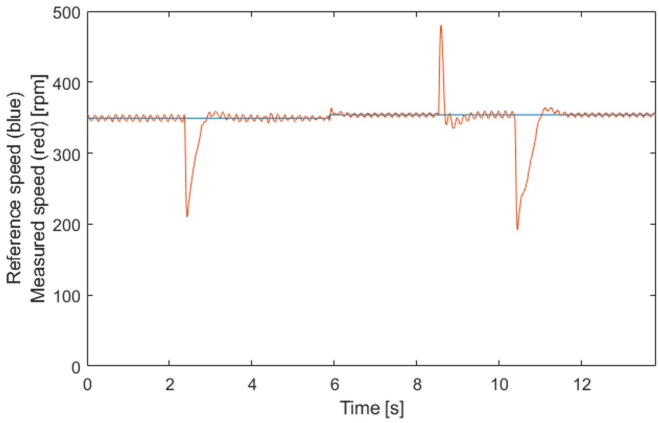

Fig. 28. Full-load step at 350 r/min (HF method). Speed reference to 355 r/min (RFO method), no-load and full-load steps.

Please note that with both methods the drive is able to perform a full-load step. Moreover, the speed ripple is comparable using HF and RFO methods.

Rotor position estimation is compared with the estimation of the model-based RFO (back EMF). The comparison was carried out during the load test shown in Fig. 27. As it can be seen from

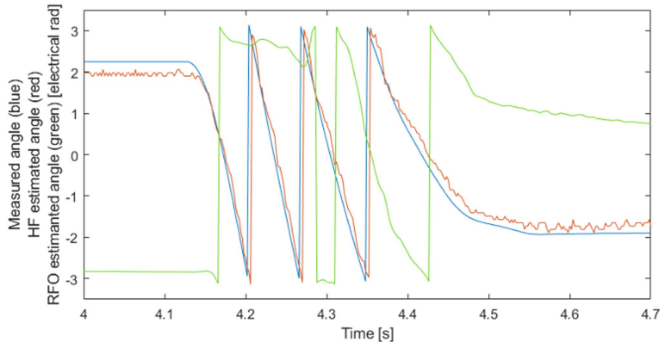

Fig. 29. Measured angle (blue), HF estimated angle (red), RFO estimated angle (green). Full-load step at standstill.

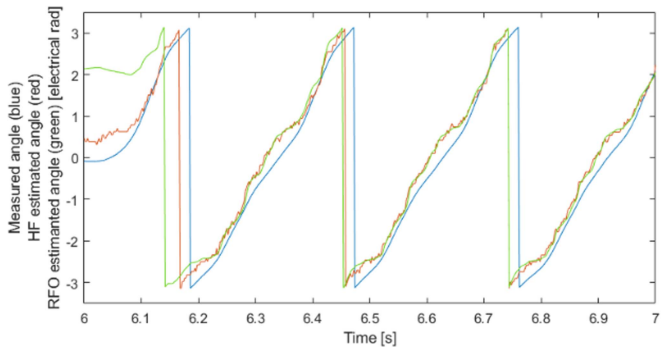

Fig. 30. Measured angle (blue), HF estimated angle (red), RFO estimated angle (green). Steady-state at 50 rpm.

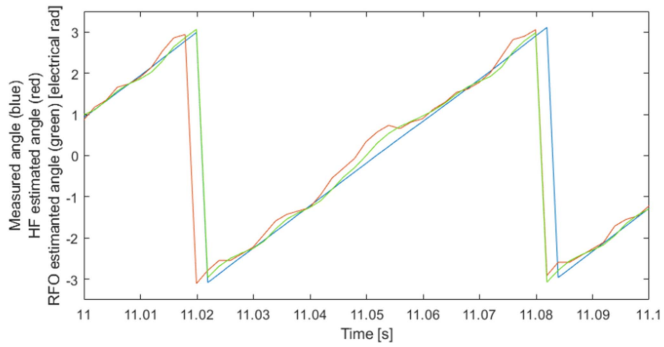

Fig. 31. Measured angle (blue), HF estimated angle (red), RFO estimated angle (green). Steady-state at 250 rpm.

Fig. 29, the RFO method does not estimate properly the angle during the load step that is imposed at a zero reference speed. At 50 r/min (see Fig. 30) the angle error obtained with RFO method is similar to the one obtained with HF method, even if it is slightly wider close to the reference speed step change, and at 250 r/min (see Fig. 31) the angle error with the RFO method is slightly lower than the angle error with the HF method. However, the RFO method is able to perform a full-load step only starting from 300 r/min; for this reason the algorithm switches to RFO estimation at 350 r/min, in order to have a sufficient safety margin for load step disturbance rejection. Speed ripple

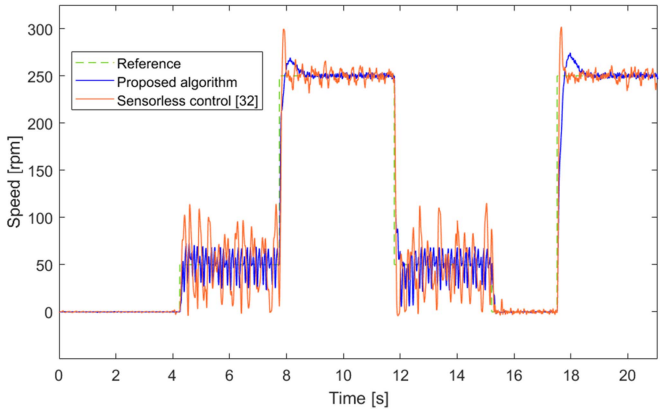

Fig. 32. Measured speed during speed steps with no-load, obtained with the proposed algorithm (blue) and with the sensorless torque control in [32] (red) on the second test bench.

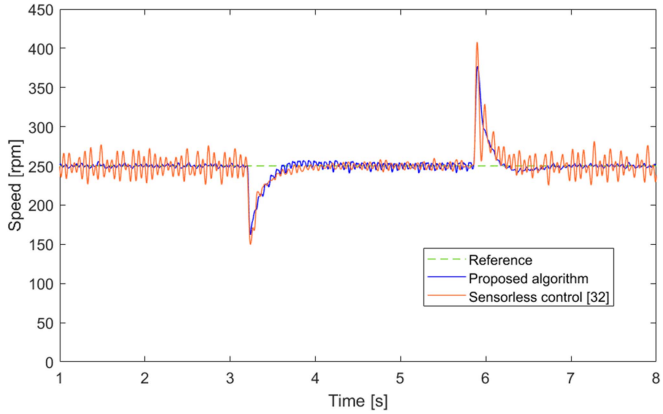

Fig. 33. Measured speed during rated load step appliance and removal at 250 r/min, obtained with the proposed algorithm (blue) and with the sensorless torque control in [32] (red) on the second test bench.

at 350 rpm with HF method and at 355 r/min with RFO method is shown in Fig. 28. Despite the difference in the angle error the speed ripple is almost the same.

G. General Validity of the Proposed Method and Comparison With the State of the Art

In this article, a particularly challenging application for sensorless switching frequency voltage injection is considered. The critical aspects are as follows.

1) Low anisotropy ratio (about 10% at 5 kHz). In the considered motor, the permanent magnets are directly mounted on a symmetric rotor, therefore the anisotropy ratio is quite low and it is comparable with the other ratio values found in the technical literature (9.8% in [32], 15% in [33]).
2) Relatively low-switching frequency (5 kHz).
3) Elevate dead times (4 μs).
4) Current measures performed with two industrial standard LEM sensors.

Since it is proven that the proposed algorithm works in these conditions, it is expected that this method can work with good performance in the majority of industrial applications.

To evaluate the validity of the proposed method, a comparison with an algorithm which is representative of the state of the art has been performed. The sensorless torque control algorithm described in [32] was chosen for this test, as it is characterized by a low torque ripple and it was therefore considered by the authors as one of the most promising in the technical literature. Both the algorithms are tested in the same conditions on the second test bench, which is equipped with a load cell to measure the motor torque ripple in the two cases. First, a low-speed test with no-load, similar to the one described in Section IV-C, has been carried out. The reference speed is set to 50 and then to 250 r/min. Fig. 32 shows the comparison between the results obtained with the sensorless torque control in [32] and with the proposed algorithm. As it can be easily noticed from the graphs, the proposed method is characterized by a significantly lower speed ripple at both speed levels.

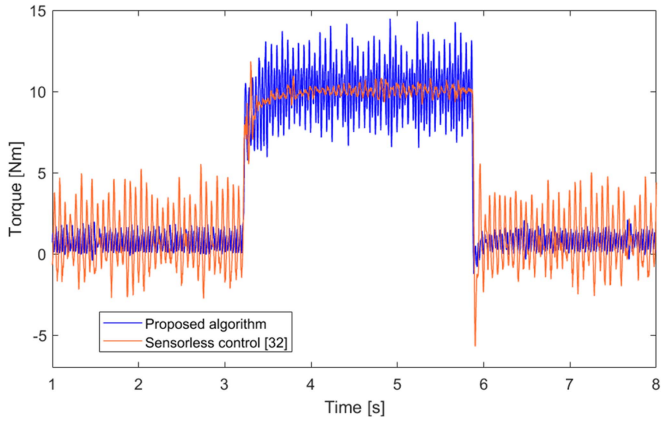

Fig. 34. Measured torque during rated load step appliance and removal at 250 r/min, obtained with the proposed algorithm (blue) and with sensorless torque control in [32] (red) on the second test bench.

Then, full-load tests were carried out using both algorithms. Figs. 33 and 34 show the speed and the measured torque, respectively, obtained applying and removing a full-load torque step to both algorithms, as the reference speed is kept equal to 250 r/min. As it can be seen from the figures, both algorithms react well to the load step at 250 r/min, showing a comparable speed ripple at full load. The speed and torque ripple before the appliance of the load step are larger in the case of the sensorless torque control in [32], though it has a lower torque ripple at rated load.

Figs. 35 and 36 show the speed and the measured torque, respectively, obtained after applying and removing a full load step at very low speed (50 r/min) to both algorithms. The proposed algorithm shows a generally more stable performance at very low speed, with smaller speed and torque ripples when the rated torque is applied. Moreover, the speed overshoot obtained with the proposed algorithm when the load is removed is much lower than in the case of the sensorless control torque in [32].

Finally, an acoustic measurement is carried out to evaluate the intensity of the motor noise with both algorithms. The noise is

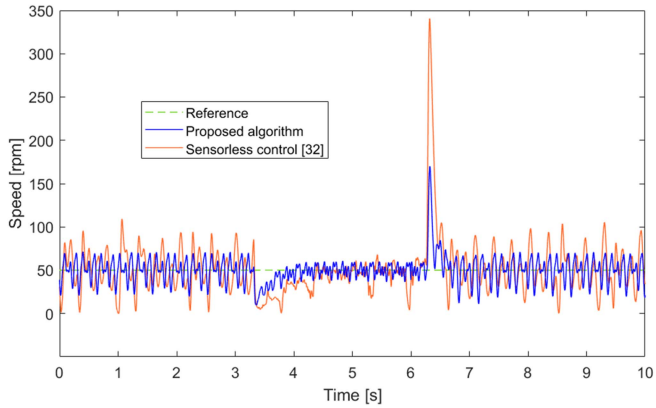

Fig. 35. Measured speed during rated load step appliance and removal at 50 r/min, obtained with the proposed algorithm (blue) and with the sensorless torque control in [32] (red) on the second test bench.

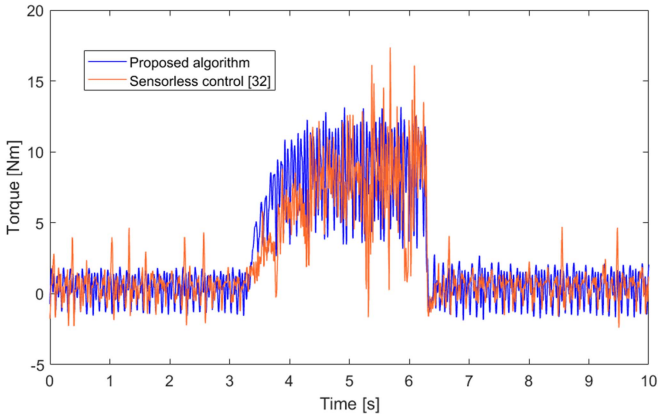

Fig. 36. Measured torque during rated load step appliance and removal at 50 r/min, obtained with the proposed algorithm (blue) and with sensorless torque control in [32] (red) on the second test bench.

measured while the motor is rotating at 250 r/min with full load torque applied, evaluated at 0.8 m from the motor. The results of the measurements are:

1) Background noise: 38 dB
2) Sensorless torque control [32]: 53 dB
3) Proposed algorithm: 49 dB

V. Conclusion

A high-frequency voltage injection sensorless algorithm is considered in this article. In particular, a square wave at the switching frequency is injected, in order to minimize the voltage injection disadvantages, the main of which is the acoustic noise. The algorithm is applied to SPMSMs, which are characterized by a low anisotropy ratio and, therefore, the signal-to-noise ratio of such sensorless algorithms is significantly low. The experimental tests show the impossibility of using a double sample approach (e.g., two current samples per PWM period), which is usually used for IPMSM. On the contrary, the oversampling method proposed in this article shows a good angle estimation and an FOC is implemented using the proposed technique. The proposed sensorless algorithm demonstrates a good response both with no-load and full-load; the stability is kept also during load steps and the speed loop bandwidth is about 5 Hz. A parallel comparison between the proposed algorithm and a state-of-art injection sensorless algorithm (presented in [32]) has been also carried out, showing a better response of the proposed algorithm in terms of torque and speed in most of the tests.

References

[1] B. Du, S. Wu, S. Han, and S. Cui, "Application of linear active disturbance rejection controller for sensorless control of internal permanent-magnet synchronous motor," *IEEE Trans. Ind. Electron.*, vol. 63, no. 5, pp. 3019–3027, May 2016.

[2] L. Qu, W. Qiao, and L. Qu, "An enhanced linear active disturbance rejection rotor position sensorless control for permanent magnet synchronous motors," *IEEE Trans. Power Electron.*, vol. 35, no. 6, pp. 6175–6184, Jun. 2020.

[3] Y. Park and S. K. Sul, "Sensorless control method for PMSM based on frequency-adaptive disturbance observer," *IEEE J. Emerg. Sel. Topics Power Electron.*, vol. 2, no. 2, pp. 143–151, Jun. 2014.

[4] N. K. Quang, N. T. Hieu, and Q. P. Ha, "FPGA-based sensorless PMSM speed control using reduced-order extended Kalman filters," *IEEE Trans. Ind. Electron.*, vol. 61, no. 12, pp. 6574–6582, Dec. 2014.

[5] S. Bolognani, L. Tubiana, and M. Zigliotto, "Extended Kalman filter tuning in sensorless PMSM drives," *IEEE Trans. Ind. Appl.*, vol. 39, no. 6, pp. 1741–1747, Nov./Dec. 2003.

[6] H. Yang, R. Yang, W. Hu, and Z. Huang, "FPGA-based sensorless speed control of PMSM using enhanced performance controller based on the reduced-order EKF," *IEEE J. Emerg. Sel. Topics Power Electron.*, vol. 9, no. 1, pp. 289–301, Feb. 2021.

[7] S. Ye and X. Yao, "An enhanced SMO-based permanent-magnet synchronous machine sensorless drive scheme with current measurement error compensation," *IEEE J. Emerg. Sel. Topics Power Electron.*, vol. 9, no. 4, pp. 4407–4419, Aug. 2021.

[8] D. Liang, J. Li, and R. Qu, "Sensorless control of permanent magnet synchronous machine based on second-order sliding-mode observer with online resistance estimation," *IEEE Trans. Ind. Appl.*, vol. 53, no. 4, pp. 3672–3682, Jul./Aug. 2017.

[9] Q. An, J. Zhang, Q. An, X. Liu, A. Shamekov, and K. Bi, "Frequency-adaptive complex-coefficient filter-based enhanced sliding mode observer for sensorless control of permanent magnet synchronous motor drives," *IEEE Trans. Ind. Appl.*, vol. 56, no. 1, pp. 335–343, Jan./Feb. 2020.

[10] J. Choi, K. Nam, A. A. Bobtsov, A. Pyrkin, and R. Ortega, "Robust adaptive sensorless control for permanent-magnet synchronous motors," *IEEE Trans. Power Electron.*, vol. 32, no. 5, pp. 3989–3997, May 2017.

[11] J. Choi, K. Nam, A. A. Bobtsov, and R. Ortega, "Sensorless control of IPMSM based on regression model," *IEEE Trans. Power Electron.*, vol. 34, no. 9, pp. 9191–9201, Sep. 2019.

[12] Y. Jeong, R. D. Lorenz, T. M. Jahns, and S.-K. Sul, "Initial rotor position estimation of an interior permanent-magnet synchronous machine using carrier-frequency injection methods," *IEEE Trans. Ind. Appl.*, vol. 41, no. 1, pp. 38–45, Jan./Feb. 2005.

[13] J. M. Liu and Z. Q. Zhu, "Novel sensorless control strategy with injection of high-frequency pulsating carrier signal into stationary reference frame," *IEEE Trans. Ind. Appl.*, vol. 50, no. 4, pp. 2574–2583, Jul./Aug. 2014.

[14] G. Wang, D. Xiao, G. Zhang, C. Li, X. Zhang, and D. Xu, "Sensorless control scheme of IPMSMs using HF orthogonal square-wave voltage injection into a stationary reference frame," *IEEE Trans. Power Electron.*, vol. 34, no. 3, pp. 2573–2584, Mar. 2019.

[15] J. H. Jang, S. K. Sul, J. I. Ha, K. Ide, and M. Sawamura, "Sensorless drive of surface-mounted permanent-magnet motor by high-frequency signal injection based on magnetic saliency," *IEEE Trans. Ind. Appl.*, vol. 39, no. 4, pp. 1031–1039, Jul./Aug. 2003.

[16] X. Luo, Q. Tang, A. Shen, and Q. Zhang, "PMSM sensorless control by injecting HF pulsating carrier signal into estimated fixed-frequency rotating reference frame," *IEEE Trans. Ind. Electron.*, vol. 63, no. 4, pp. 2294–2303, Apr. 2016.

[17] N. Bianchi, S. Bolognani, J. H. Jang, and S.-K. Sul, "Comparison of PM motor structures and sensorless control techniques for zero-speed rotor position detection," *IEEE Trans. Power Electron.*, vol. 22, no. 6, pp. 2466–2475, Nov. 2007.

[18] M. A. G. Moghadam and F. Tahami, "Sensorless control of PMSMs with tolerance for delays and stator resistance uncertainties," *IEEE Trans. Power Electron.*, vol. 28, no. 3, pp. 1391–1399, Mar. 2013.

[19] G. Foo and M. F. Rahman, "Sensorless sliding-Mode MTPA control of an IPM synchronous motor drive using a sliding-mode observer and HF signal injection," *IEEE Trans. Ind. Electron.*, vol. 57, no. 4, pp. 1270–1278, Apr. 2010.
[20] Z. Lin, X. Li, Z. Wang, T. Shi, and C. Xia, "Minimization of additional high-frequency torque ripple for square-wave voltage injection IPMSM sensorless drives," *IEEE Trans. Power Electron.*, vol. 35, no. 12, pp. 13345–13355, Dec. 2020.
[21] Y. D. Yoon, S. K. Sul, S. Morimoto, and K. Ide, "High-bandwidth sensorless algorithm for AC machines based on square-wave-type voltage injection," *IEEE Trans. Ind. Appl.*, vol. 47, no. 3, pp. 1361–1370, May/Jun. 2011.
[22] H. Zhang, W. Liu, Z. Chen, G. Luo, J. Liu, and D. Zhao, "Asymmetric space vector modulation for PMSM sensorless drives based on square-wave voltage-injection method," *IEEE Trans. Ind. Appl.*, vol. 54, no. 2, pp. 1425–1436, Mar./Apr. 2018.
[23] X. Wu et al., "Initial rotor position detection for sensorless interior PMSM with square-wave voltage injection," *IEEE Trans. Magn.*, vol. 53, no. 11, Nov. 2017, Art. no. 8112104.
[24] S. Kim, J.-I. Ha, and S.-K. Sul, "PWM switching frequency signal injection sensorless method in IPMSM," *IEEE Trans. Ind. Appl.*, vol. 48, no. 5, pp. 1576–1587, Sep./Oct. 2012.
[25] C.-E. Hwang, Y. Lee, and S.-K. Sul, "Analysis on position estimation error in position-sensorless operation of IPMSM using pulsating square wave signal injection," *IEEE Trans. Ind. Appl.*, vol. 55, no. 1, pp. 458–470, Jan./Feb. 2019.
[26] B. Weber, G. Lindemann, and A. Mertens, "Reduced observer for anisotropy-based position estimation of PM synchronous machines using current oversampling," in *Proc. IEEE Int. Symp. Sensorless Control Elect. Drives*, 2017, pp. 121–126.
[27] P. Landsmann, J. Jung, M. Kramkowski, P. Stolze, D. Paulus, and R. Kennel, "Lowering injection amplitude in sensorless control by means of current oversampling," in *Proc. 3rd IEEE Int. Symp. Sensorless Control Elect. Drives*, 2012, pp. 1–6.
[28] M. Giuliato, L. Peretti, F. Tinazzi, and M. Zigliotto, "Sensorless control for a synchronous reluctance motor based on current oversampling using standard PWM excitation," in *Proc. 10th Int. Conf. Power Electron., Mach. Drives*, 2020, pp. 13–18.
[29] B. Weber, K. Wiedmann, and A. Mertens, "Increased signal-to-noise ratio of sensorless control using current oversampling," in *Proc. 9th Int. Conf. Power Electron. Energy Convers. Congr. Expo. Asia*, 2015, pp. 1129–1134.
[30] L. M. Gong and Z. Q. Zhu, "Robust initial rotor position estimation of permanent-magnet brushless AC machines with carrier-signal-injection-based sensorless control," *IEEE Trans. Ind. Appl.*, vol. 49, no. 6, pp. 2602–2609, Nov./Dec. 2013.
[31] A. Benevieri, M. Marchesoni, M. Passalacqua, and L. Vaccaro, "Experimental low-speed performance evaluation and comparison of sensorless passive algorithms for SPMSM," *IEEE Trans. Energy Convers.*, vol. 37, no. 1, pp. 654–664, Mar. 2022.
[32] P. Landsmann and R. Kennel, "Saliency-based sensorless predictive torque control with reduced torque ripple," *IEEE Trans. Power Electron.*, vol. 27, no. 10, pp. 4311–4320, Oct. 2012.
[33] D. Paulus, P. Landsmann, and R. Kennel, "Sensorless field- oriented control for permanent magnet synchronous machines with an arbitrary injection scheme and direct angle calculation," in *Proc. Symp. Sensorless Control Elect. Drives*, 2011, pp. 41–46.

Alessandro Benevieri was born in Genoa, Italy in 1995. He received the B.S. and the M.S. (Hons.) degrees in electrical engineering in 2017 and 2020, respectively, from the University of Genoa, Genoa, Italy, where he is currently working toward the Ph.D. degree in electrical engineering with the Department of Electrical, Electronic and Telecommunication Engineering and Naval Architecture.

His research interests include power converters and control for electrical drives.

Andrea Formentini (Member, IEEE) received the M.S. degree in computer engineering and the Ph.D. degree in electrical engineering from the University of Genova, Genova, Italy, in 2010 and 2014 respectively.

He was a Research Fellow with the Power Electronics, Machines and Control Group, University of Nottingham, Nottingham, U.K. In September 2018, he was an Assistant Professor with the University of Nottingham. In 2021, he was a Lecturer in engineering science with the University of Oxford. He is currently a Lecturer with University of Genoa, where he pursues research in control of electric drives and power electronics.

Mario Marchesoni (Member, IEEE) received the M.S. (Hons.) degree in electrical engineering and the Ph.D. degree in electrical engineering in power electronics from the University of Genova, Genova, Italy, in 1986 and 1990, respectively.

Following his graduation, he began his research activity with the Department of Electrical Engineering, University of Genova, where he was an Assistant Professor from 1992 to 1995. From 1995 to 2000, he was with the Department of Electric and Electronic Engineering, University of Cagliari, Cagliari, Italy, where he was a Full Professor of power industrial electronics. Since 2000, he has been with the University of Genova, where he is currently a Full Professor of electrical drives control. His research interests include power electronics, with particular reference to high power systems for grid and motor applications, electrical systems for transportation, electrical drives, electrical machines, and automatic control. His technical and scientific activity, certified by about 220 papers mainly presented at international conferences and published on international journals, has been carried out within research contracts and co-operations with national and international companies.

Dr. Marchesoni was the General Chairman of the 21st European Conference on Power Electronics and Applications.

Massimiliano Passalacqua (Member, IEEE) was born in Genoa, Italy in 1993. He received the B.S. (Hons.), M.S. (Hons.), and Ph.D. degrees in electrical engineering from the University of Genoa, Genoa, Italy, in 2015, 2017, and 2021, respectively.

He is currently a Research Fellow with the Department of Electrical, Electronic and Telecommunication Engineering and Naval Architecture, University of Genoa. His research interests include power electronics, control for electrical drives, and hybrid electric vehicles.

Luis Vaccaro (Member, IEEE) was born in Chile. He received the B.Sc. degree in theoretical physics from the University of Concepcion, Concepcion, Chile, in 1991, and the M.Sc. degree in nuclear physics and the Ph.D. degree in electrical engineering from the University of Genoa, Genova, Italy, in 1995 and 2009, respectively.

In 2004, he joined the team of power electronics with the University of Genoa. His primary research interests include multilevel converters, predictive control, hybrid electric vehicles, and renewable energies.

Open Access funding provided by 'Università degli Studi di Genova' within the CRUI CARE Agreement